

Characterization of the Si:Se⁺ spin-photon interface

Adam DeAbreu,¹ Camille Bowness,¹ Rohan J. S. Abraham,¹ Albeta Medvedova,¹ Kevin J. Morse,¹ Helge Riemann,² Nikolay V. Abrosimov,² Peter Becker,³ Hans-Joachim Pohl,⁴ Michael L. W. Thewalt,¹ and Stephanie Simmons^{1,*}

¹*Department of Physics, Simon Fraser University, Burnaby, British Columbia V5A 1S6, Canada*

²*Leibniz-Institut für Kristallzüchtung, 12489 Berlin, Germany*

³*Physikalisch-Technische Bundesanstalt (PTB) Braunschweig, 38116 Braunschweig, Germany*

⁴*VITCON Projectconsult GmbH, 07745 Jena, Germany*

(Dated: March 13, 2022)

Silicon is the most developed electronic and photonic technological platform and hosts some of the highest-performance spin and photonic qubits developed to date. A hybrid quantum technology harnessing an efficient spin-photon interface in silicon would unlock considerable potential by enabling ultra-long-lived photonic memories, distributed quantum networks, microwave to optical photon converters, and spin-based quantum processors, all linked using integrated silicon photonics. However, the indirect bandgap of silicon makes identification of efficient spin-photon interfaces non-trivial. Here we build upon the recent identification of chalcogen donors as a promising spin-photon interface in silicon. We determined that the spin-dependent optical degree of freedom has a transition dipole moment stronger than previously thought (here 1.96(8) Debye), and the T_1 spin lifetime in low magnetic fields is longer than previously thought ($> 4.6(1.5)$ hours). We furthermore determined the optical excited state lifetime (7.7(4) ns), and therefore the natural radiative efficiency (0.80(9) %), and by measuring the phonon sideband, determined the zero-phonon emission fraction (16(1) %). Taken together, these parameters indicate that an integrated quantum optoelectronic platform based upon chalcogen donor qubits in silicon is well within reach of current capabilities.

I. INTRODUCTION

A future quantum technology, wherein stored quantum information is communicated over a quantum network, will necessarily involve both matter-based qubits and optical photons. In pursuit of this aim, many potential spin-photon interfaces are being actively developed [1–3]. A wide array of defects in semiconductors and insulators have attracted attention because of their favourable optical and spin characteristics. These include quantum dots in III-V heterostructures [4], nitrogen-vacancy [5] and silicon-vacancy [6] centers in diamond, rare-earth ions in insulators such as Nd:YSO [7] and Er:YSO [8], defects in SiC [9, 10], and even recent work on donors in ZnO [11]. Notable in its absence from this list is silicon, which, when isotopically purified to ^{28}Si , is host to some of the longest-lived and highest-fidelity spin qubits studied to date [12–15]. Silicon offers high performance integrated single photon detectors [16] in addition to an expansive selection of high quality photonic components [17, 18] due to decades of fabrication process development. Furthermore, silicon has a strong $\chi^{(3)}$ nonlinearity and large refractive index that enables dense packing of photonic circuitry. Despite the considerable advantages of these two quantum silicon platforms, unifying these technologies through an efficient spin-photon interface has proven elusive.

A few paramagnetic centres in silicon possess spin-dependent optical transitions, including shallow donor-bound excitons [19] and orbital transitions in rare earth ions, such as erbium [20]. However, in the aforementioned

cases, the defects only weakly couple to light as determined by their small optical transition dipole moments. Although recent work has demonstrated evanescent coupling of defects with strong transition dipole moments in materials placed adjacent to silicon photonic structures [21], the coupling strengths and photon collection efficiencies are inherently limited in such designs.

The ideal silicon spin-photon interface would be a natively-integrated optical center which possess a long-lived spin, a high transition dipole moment, and a high radiative efficiency. In this work we demonstrate that singly-ionized deep chalcogen donors in silicon possess a strong light-matter interaction, suitable for strong coupling to silicon photonic cavities at the single-spin level. This offers a clear path towards chalcogen-based integrated silicon quantum optoelectronics.

The optical characteristics of substitutional chalcogen donors (specifically sulfur, selenium, and tellurium) have been studied for decades [22–26]. It was identified that the natural distribution of silicon and chalcogen isotopes act as sources of static inhomogeneity in the bulk. Consequently, ultra-sharp optical linewidths, on the order of μeV can be achieved [26] by working with ensembles of individual chalcogen isotopes in isotopically purified ^{28}Si . This remarkable uniformity allowed for the hyperfine splitting and the electron spin g-value of the $1s:A$ ground state of singly-ionized ^{77}Se to be directly observed through optical excitation into the first excited state, $1s:T_2:\Gamma_7$. Following this, initial electron spin characterization at X-band microwave frequencies on $^{77}\text{Se}^+$ demonstrated promising electron spin qubit coherence and lifetime characteristics [27] similar to that of the shallow donors' ultra-long lived electron spins.

The identification of singly-ionized chalcogen donors as a promising spin-photon interface in silicon was only

* Corresponding author: s.simmons@sfu.ca

made relatively recently [28], and bounds on some key spin and optical parameters of $^{77}\text{Se}^+$ were determined to support this proposal. Key parameters in Ref. [28] included a lower bound on the spin T_1 lifetime ($> 6.2(4)$ minutes) as well as lower bounds on the optical transition dipole moment (> 0.77 Debye), optical excited state lifetime (> 5.5 ns), as well as an upper bound on the calculated radiative lifetime (< 39 μs). In this work we improve upon the bounds on all of these key parameters, including the spin T_1 time ($> 4.6(1.5)$ hours) and the transition dipole moment ($1.96(8)$ Debye). Furthermore, we offer new insights into the optical transition of interest by reporting the phonon sideband profile and zero phonon line (ZPL) fraction ($16(1)$ %) and a direct measurement of the excited state lifetime ($7.7(4)$ ns), and hence the total radiative efficiency ($0.80(9)$ %). Lastly, we precisely determine the location of the second excited state in the neutral charge state of Se by performing Raman spectroscopy. The experimental results presented in Section II are structured in that order.

A. The $^{28}\text{Si}:^{77}\text{Se}^+$ spin-photon system

Substitutional selenium atoms in silicon are deep double donors. When singly ionized, the unpaired spin- $\frac{1}{2}$ electron possesses a hydrogenic orbital structure with a 1s ground state. The sixfold degeneracy of the conduction band and the two electron spin states give rise to twelve 1s levels which are split by a combination of central cell, valley-orbit, and spin-orbit effects. The spin and photon degrees of freedom relevant to this work are all contained within these twelve electronic 1s levels.

The ground state, 1s:A, possesses two degenerate electron spin levels and has a binding energy of ~ 593 meV [24]. The first orbital excited states, labeled 1s:T₂, are split into components labeled 1s:T₂: Γ_7 and 1s:T₂: Γ_8 , the lower of which, 1s:T₂: Γ_7 , possesses two spin-orbit levels and has a binding energy of ~ 166 meV [24]. The remaining 1s levels, labeled 1s:E, are thought to lie above 1s:T₂: Γ_8 , as is the case for the neutral charge state Se^0 and the group V shallow donors, but have not been observed in Se^+ . The optical transitions between 1s:A and 1s:T₂: Γ_7 are forbidden according to effective mass theory (EMT) but are symmetry-allowed, and approximately 427 meV, or 2.9 μm , [24] which is in the mid-infrared optical band. Further details on the orbital structure of this system are given in Ref. [28] and references therein.

Additionally, the $^{77}\text{Se}^+$ isotope possesses a spin- $\frac{1}{2}$ nuclear spin and a corresponding $A \approx 1.66$ GHz hyperfine [26, 28] interaction within the 1s:A electronic manifold. This gives rise to a ground state spin Hamiltonian shared by that of the neutral shallow donor ^{31}P and given by

$$\mathcal{H} = \frac{g_e \mu_B}{h} B_0 S_z - \frac{g_n \mu_N}{h} B_0 I_z + A \vec{S} \cdot \vec{I}, \quad (1)$$

where A , the hyperfine constant, and g_e (2.0057) and g_n (1.07), the electron and nuclear g -factors respectively,

are specific to $^{77}\text{Se}^+$. Here μ_B and μ_N are the Bohr and nuclear magnetons, h is the Planck constant, and \vec{S} and \vec{I} are the spin operators of the electron and nucleus. At zero magnetic field, this spin Hamiltonian results in split 1s:A energy levels defined by electron-nuclear spin singlet and triplet states. The 1s:T₂: Γ_7 state possesses no such splitting and therefore these levels form a lambda transition [24] which can be spectrally resolved in the bulk [26, 28]. The allowed magnetic resonance transitions from the singlet state S_0 to the triplet states T_- , T_0 , T_+ support long lived qubits [28], particularly across the $S_0 \Leftrightarrow T_0$ transition which is a ‘clock transition’ [29] at zero field.

II. EXPERIMENTAL RESULTS

A. Singlet-triplet T_1 temperature dependence

The spin equilibration time constant, T_1 , of the $^{77}\text{Se}^+$ singlet/triplet qubit in Earth’s magnetic field and at low temperatures (1.6 K) was previously found to be approximately 6 minutes [28]. Although already quite long, this T_1 time is shorter than the ~ 30 minute electron T_1 of ^{31}P measured at 1.6 K and 0.35 T, as well as significantly shorter than the projected electron T_1 times available to ^{31}P at 1.6 K in Earth’s magnetic field [30]. Six minutes is substantially longer than previously measured $^{77}\text{Se}^+$ electron T_1 times collected at higher temperatures [27], but shorter than the ~ 337 hour projected T_1 time following a T^9 dependence fitted from this higher-temperature data and extrapolated to 1.6 K (See Fig 1). Here we elucidate the decay mechanisms affecting the $^{77}\text{Se}^+$ singlet/triplet qubit and determine an experimental regime which gives rise to a 276(90) minute (4.6(1.5) hour) T_1 time.

The similarities between the ^{31}P and $^{77}\text{Se}^+$ systems imply that a number of known ^{31}P electron T_1 decay mechanisms, such as the direct [30], Raman [31], and concentration-dependent decay mechanisms with concentrations above 10^{16} cm^{-3} [30], can apply to $^{77}\text{Se}^+$. The significantly larger valley-orbit splitting between the ground 1s:A and first excited states 1s:T₂: Γ_7 of $^{77}\text{Se}^+$ – at least seven times greater than the maximum phonon energy – implies that the Orbach [32] decay mechanism known to apply to ^{31}P is irrelevant to $^{77}\text{Se}^+$.

An additional decay mechanism is known [28] to contribute to the T_1 decay of $^{77}\text{Se}^+$: incident room-temperature blackbody radiation possesses sufficient energy to ionize both neutral and singly-ionized ^{77}Se , directly effecting T_1 via time-varying local charge configurations. Under our experimental conditions, blackbody radiation generated within the cryogenic apparatus is negligible compared to the room temperature incident blackbody radiation optically coupled to the sample. Correspondingly, this blackbody T_1 decay mechanism is largely independent of the sample temperature. In contrast, the direct and Raman decay mechanisms display a $1/T$ and $1/T^9$ temperature dependence, respec-

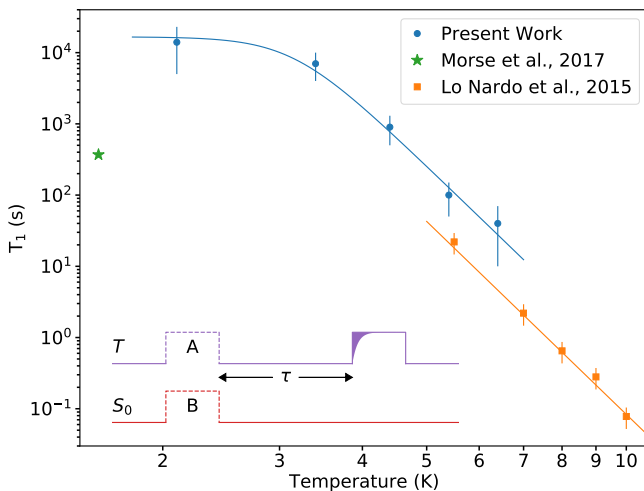


Fig. 1. Temperature dependence of $^{77}\text{Se}^+$ electron-nuclear spin singlet/triplet T_1 taken near Earth’s magnetic field (blue), revealing a low temperature limit of $T_1 = 4.6(1.5)$ hours, and comparison with published data, collected with less blackbody shielding (green) reprinted from Ref. [28] with permission, as well as electron spin T_1 data taken at 0.35 T (orange) reprinted from Ref. [27] with permission. (Inset) Schematic diagram of optical pumping and readout sequence to measure singlet/triplet T_1 . For a given wait time, τ , the total remaining polarization signal is measured as the difference between two integrated absorption transient areas, both measuring the population of the triplet state (solid), after two different initialization pulses (dashed). First (A) after initializing into the singlet by pumping on the $1s:A:T \Leftrightarrow 1s:T_2:\Gamma_7$ transition, here labeled T , and secondly (B) after initializing into the triplet by pumping on the $1s:A:S_0 \Leftrightarrow 1s:T_2:\Gamma_7$ transition, here labelled S_0 .

tively [30, 31]. Measurements of the electron T_1 in a low-concentration ($\sim 2 \times 10^{13} \text{ cm}^{-3}$) $^{77}\text{Se}^+$ bulk sample (sample $^{28}\text{Si}:\text{Se}:\text{LB}$, see Supplementary Materials [33]) as a function of temperature were used to determine the prevalence of these possible mechanisms.

In order to minimize room temperature blackbody effects, optical bandpass filters centered at $2.9 \mu\text{m}$ as well as neutral density filters were mounted within the cryogenic assembly in the optical beam path, and the sample was shielded from room temperature blackbody radiation from all other directions.

The singlet/triplet qubit was initialized by resonantly pumping one arm of the lambda transition, for example initializing into the singlet state by selectively pumping $1s:A:T \Leftrightarrow 1s:T_2:\Gamma_7$, as described in Ref. [28]. Following this, a mechanical shutter blocked the resonant light. After a chosen delay, the remaining spin hyperpolarisation was measured by recording the absorption transient of unblocked resonant light (see Fig. 1 inset). For a given delay time, two different measurements were taken and the difference between their absorption transients constituted the measured signal. The first of these measurements hyperpolarised into the singlet state and the second into the triplet state. Both measurements’ absorp-

tion transients consistently probed the final triplet population. This subtraction method ensured that the signal would necessarily decay to zero in the long delay limit where the spins reached equilibrium. The singlet/triplet T_1 lifetime at a given temperature was determined by iterating this measurement with variable delay times.

The temperature dependence of T_1 over the range 2.1 to 6.4 K is shown in Fig. 1. The data is well fit by $1/T_1 = AT^9 + B$, with $A = 2.0(3) \times 10^{-9} \text{ s}^{-1}\text{K}^{-9}$ and a temperature independent contribution with a low temperature limit of $T_1 = 4.6(1.5)$ hours, representing a T^9 Raman process and most likely a residual blackbody-related decay process dominating below 2 K. This T^9 Raman process is in agreement with Ref. [27] taken at 0.35 T, which is fit well by $1/T_1 = CT^9$ ($C = 1.2 \times 10^{-8} \text{ s}^{-1}\text{K}^{-9}$). The disagreement near 5 K may be due to temperature offsets between these two different experimental setups; alternatively, although the T^9 relaxation process is expected to be independent of magnetic field for electron spins [31], this may not apply when comparing between singlet/triplet spin qubits and nearly pure electron spin qubits. These trends indicate that a spin T_1 of 19 ± 3 minutes is available at the easily accessible temperature of 4.2 K.

B. Absorption

In this section we present measurements based on optical absorption spectra. We improve upon previous transition dipole moment estimates, and use this data to provide a concentration conversion factor.

1. Transition dipole moment

The optical interaction strength of a spin-photon interface is characterized by its transition dipole moment, μ . The dipole moment can be calculated from absorption spectra of a bulk sample, combined with an accurate defect concentration value, and a known optical path length [33]. Previous work [28] employed a bulk sample with non-uniform $^{77}\text{Se}^+$ concentration and consequently only lower bounds on the transition dipole moment could be made.

Here we calculate the transition dipole moment using a selenium diffused, $^{28}\text{Si}:\text{Se}$, wafer sample (sample $^{28}\text{Si}:\text{Se}:\text{IB}$, see Supplementary Materials [33]). An absorption spectrum was measured using a Bruker IFS 125HR Fourier transform infrared (FTIR) spectrometer with gold mirrors, a KBr beamsplitter, and a mercury-cadmium-telluride (MCT) detector to obtain an absorption coefficient spectrum of the $\text{Se}^+ 1s:A \Rightarrow 1s:T_2:\Gamma_7$ transition. Where the absorption coefficient spectrum is calculated according to:

$$\alpha = \frac{-1}{L} \ln \left(\frac{I_s}{I_0} \right), \quad (2)$$

where I_s and I_0 are FTIR spectra with and without the sample in the beam path, respectively, and L is the length of the sample.

This sample was confirmed to have a near-uniform $[\text{Se}^+]$ concentration by observing the complete compensation of all boron in the sample [33]. In this case one might expect $[\text{B}] = [\text{Se}^+]$ throughout the sample, however, the precise distribution of donors and acceptors in the sample may modify this value. To measure $[\text{Se}^+]$ precisely, we applied a tip-angle measurement [13], whose details have been described in Ref [28]. We measured $[\text{Se}^+] = 5.2(4) \times 10^{14} \text{ cm}^{-3}$ which is less than the measured $[\text{B}]$ of $5.9(8) \times 10^{14} \text{ cm}^{-3}$, likely indicating the presence of doubly ionized selenium, Se^{2+} , or ionized selenium pairs, $\text{Se}_2^{+/2+}$. Combining this with the absorption coefficient spectrum we calculate a transition dipole moment of $\mu = 1.96(8)$ Debye [33]. This value is more than a factor of 2 higher than the previously established lower bound.

2. Selenium conversion factor

From the tip-angle concentration and absorption coefficient spectrum we determined a conversion factor,

$$f = \frac{[\text{Se}^+]}{\int \alpha d\nu} = 6.2(5) \times 10^{14} \text{ cm}^{-1}, \quad (3)$$

for the $1s:A \Rightarrow 1s:T_2:\Gamma_7$ zero phonon spectral line, where $\int \alpha d\nu$ is the integrated absorption coefficient spectra of the zero phonon spectral line. Peak conversion factors, $k_{\text{Se}^+} = [\text{Se}^+]/\alpha_{\text{max}}$, are tabulated in the Supplementary Materials [33].

C. Photoluminescence

The radiative properties – both the radiative efficiency and the zero phonon line fraction – of the Se^+ spin-photon interface have not been previously established. In this section we report the observation of the phonon-assisted luminescence sideband of the $1s:T_2:\Gamma_7 \Rightarrow 1s:A$ optical transition, which reveals a zero phonon line fraction of 16(1) %. Subsequently we measured the excited state lifetime (7.7(4) ns) and compared this with the calculated radiative lifetime to infer a radiative efficiency of 0.80(9) %.

1. Zero phonon line fraction

Photoluminescence spectra were obtained using a Bruker IFS 125HR FTIR spectrometer with gold mirrors, a CaF_2 beamsplitter, and a liquid nitrogen-cooled InSb detector with a 2440 nm long pass filter. A high $[\text{Se}^+]$ sample ($w^{\text{nat}}\text{Si}:\text{nat}\text{Se}:\text{HB}$, see Supplementary Materials [33]) was pumped with 1 W of laser light resonant with the $\text{Se}^+ 1s:A \Rightarrow 2p_{\pm}$ transition (4578 cm^{-1} , or 2184 nm), which was generated using a $\text{Cr}^{2+}:\text{ZnS}/\text{Se}$

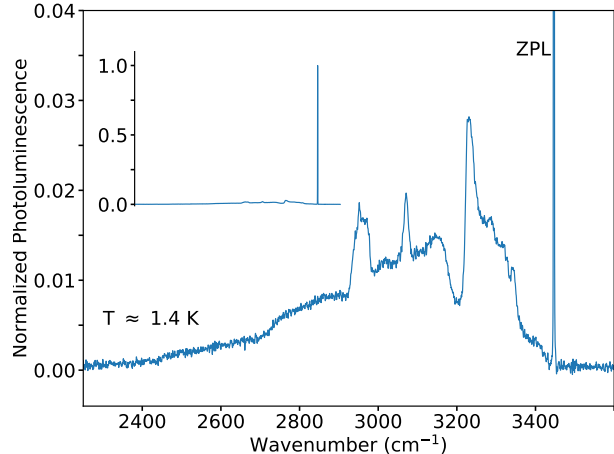


Fig. 2. The photoluminescence spectra of the $\text{Se}^+ 1s:T_2:\Gamma_7 \Rightarrow 1s:A$ transition taken with a spectral resolution of 1 cm^{-1} . (**Inset**) The normalized spectra showing the relative height of the zero phonon line (ZPL) to the phonon sideband. (**Main panel**) The same spectra, clipped vertically to display the phonon sideband features. The area of the phonon sideband is 5.6 times larger than the area of the ZPL, revealing a reabsorption-corrected ZPL fraction of 16(1) %.

narrowband tunable laser pumped by an erbium fiber laser (IPG Photonics) operating at 1567 nm. From the excited state $2p_{\pm}$, the electron can decay via phonon cascade to $1s:T_2:\Gamma_7$ followed by photon emission to $1s:A$.

The resulting photoluminescence spectrum, including the phonon-assisted sideband, is seen in Fig. 2. The integrated phonon sideband is 5.6 times larger than the area of the zero phonon line, resulting in a ZPL fraction lower bound of 15 %. After correcting for re-absorption of light given the known ZPL transition dipole moment, which will disproportionately affect the integrated area of the ZPL, we obtain a ZPL fraction of 16(1) %.

The total radiative lifetime includes both the zero-phonon and the phonon-assisted radiative pathways, resulting in a total calculated radiative lifetime of $\tau = 0.90(7) \mu\text{s}$ [33].

2. Excited state lifetime and radiative efficiency

The decay of the $1s:T_2:\Gamma_7$ valley state to the ground state $1s:A$ can occur through purely radiative, phonon-assisted radiative, and fully nonradiative pathways. The ratio of the measured $1s:T_2:\Gamma_7$ excited state lifetime to the calculated radiative lifetime reveals the technologically consequential radiative efficiency of this spin-photon interface.

Conventional methods of directly measuring a total luminescence lifetime employ optical pulses and time-resolved, high-sensitivity detectors which are at least comparable in speed with the transition lifetime of interest. Such sources and detectors are not yet routinely

available in the 2.9 μm region. Hence, previous to this work, only lower bounds on the total lifetime of this centre were known. Hole-burning measurements, limited by FTIR spectrometer resolution, indicated [28] a total excited state lifetime longer than 5.5 ns corresponding to a homogeneous linewidth smaller than 0.001 cm^{-1} .

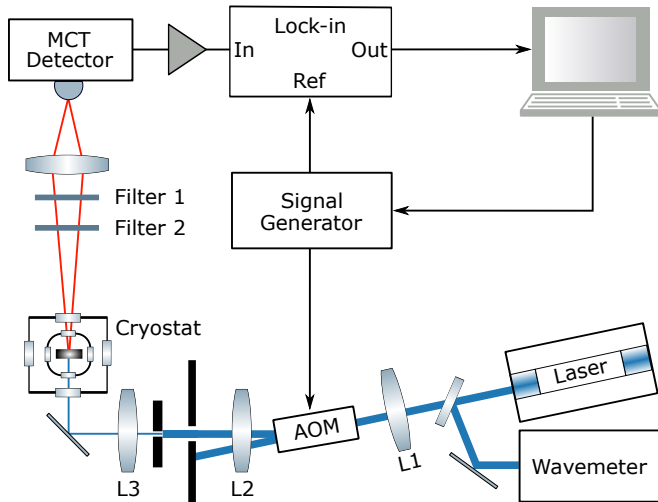


Fig. 3. Schematic of experimental set-up. A laser, tuned to the $\text{Se}^+ 1s:A \Rightarrow 2p_{\pm}$ transition (4578 cm^{-1} , or 2184 nm), whose wavelength was monitored using a pick-off beam routed into a wavemeter, was focused through a lens (L1) to minimize the beam waist within a 10 MHz bandwidth germanium acousto-optic modulator (AOM). The first diffracted (modulated) beam was recollimated (L2) and passed through a 1 mm aperture, to reject the main beam and higher order diffracted beams, and focused (L3) onto the $w^{\text{nat}}\text{Si}:n^{\text{nat}}\text{Se:HB}$ sample held in superfluid helium. A portion of the resulting $1s:T_2:\Gamma_7 \Rightarrow 1s:A$ luminescence signal was captured by an elliptical mirror and sent through 2440 nm and 2850 nm long-pass filters, Filter 1 and Filter 2, to selectively pass $1s:T_2:\Gamma_7 \Rightarrow 1s:A$ light into an MCT detector. A lock-in measurement was applied to the detected signal using the AOM driving frequency as the reference.

To directly measure the excited state lifetime, we performed a modulated excitation experiment [34] using a continuous-wave, single-frequency laser modulated by an acousto-optic modulator (AOM). The measurement configuration is shown in Fig. 3. The laser was brought into resonance with the $1s:A \Rightarrow 2p_{\pm}$ transition (4578 cm^{-1} , or 2184 nm), as in Sec. II C 1, to efficiently pump to $1s:T_2:\Gamma_7$ via the $2p_{\pm}$ state. This pump laser was sinusoidally modulated with a germanium AOM (IntraAction AGM-802A9) with a nominal bandwidth of 10 MHz, which was increased to 20 MHz by reducing the laser spot size using a converging lens pair. Approximately 400 mW of laser light was incident on the sample. The resulting $1s:T_2:\Gamma_7 \Rightarrow 1s:A$ luminescence from the sample $w^{\text{nat}}\text{Si}:n^{\text{nat}}\text{Se:HB}$ (see Supplementary Materials [33]) was spectrally filtered and detected using an MCT detector (VIGO Systems, PVI-4TE-1-0.5x0.5), and fed into a lock-in with the AOM modulation drive as its reference.

After correcting for the instrumental frequency re-

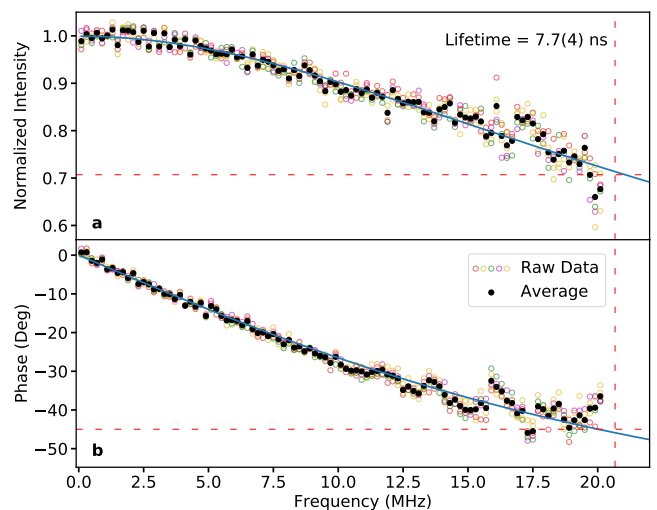


Fig. 4. Excited state lifetime measurement of the $1s:T_2:\Gamma_7$ state of Se^+ detected through modulation-frequency-dependent luminescence. Five separate datasets are plotted in open circles and their average is indicated by closed black circles. (a) Amplitude response of the photoluminescence as a function of excitation modulation frequency. The averaged amplitude data is fit with Eqn. 4 (blue curve) and the data is normalized to the fit amplitude. (b) Phase response of the photoluminescence as a function of excitation modulation frequency. The phase lag between the AOM drive signal and the luminescence signal is fit with Eqn. 5 (blue curve). Red dashed lines intersect the data at the critical modulation frequencies, at which the normalized fit amplitude has dropped to $1/\sqrt{2}$ and phase has lagged by 45° , revealing a T_1 time for the $1s:T_2:\Gamma_7$ excited state of $7.7(4)\text{ ns}$.

sponse by measuring scattered pump laser light, the frequency dependence of the resulting signal revealed the excited state lifetime. At frequencies much lower than the inverse of the excited state lifetime the system has time to equilibrate and a high AC photoluminescence signal is detected, whereas at higher frequencies the AC signal amplitude will drop. Alternatively put, the system behaves as a low-pass filter with a characteristic amplitude (A) and phase (Θ) response, as a function of modulation frequency, f , given by [34]:

$$A = \frac{1}{[1 + (2\pi f T_1)^2]^{1/2}}, \quad (4)$$

$$\Theta = -\tan^{-1}(2\pi f T_1) \quad (5)$$

where T_1 is the decay time of the optically excited state. The resulting data, corrected for the system response, are shown in Fig. 4. The characteristic amplitude and phase drop-off points, at $1/\sqrt{2}$ and 45° , agree and reveal a T_1 time for the $1s:T_2:\Gamma_7$ excited state to be $7.7(4)\text{ ns}$.

This gives a radiative efficiency of $0.80(9)\%$ when compared to the radiative lifetime of $0.90(7)\text{ }\mu\text{s}$, as well as a homogeneous linewidth of $0.00069(4)\text{ cm}^{-1}$. However, as thermally activated transitions to higher excited states are possible [28] this homogeneous linewidth is likely to be a lower bound. For the purposes of estimating cou-

pling cooperativity [33] between the $\text{Se}^+ 1s:A \Leftrightarrow 1s:T_2:\Gamma_7$ transition and a photonic cavity we use the upper bound determined by hole burning, 0.001 cm^{-1} . With a ZPL dipole moment of $\mu = 1.96(8)$ Debye, a Se^+ spin in the mode maximum of a cavity with an unloaded Q-factor of 1.5×10^4 and a modal volume, $V = (\lambda/n)^3$, would display a cooperativity of $C = 1$.

D. Raman spectroscopy

The $1s:A \Leftrightarrow 1s:T_2:\Gamma_7$ transition amounts to at least a seven phonon transition, and yet results from Sec. II C 2 show that relaxation from $1s:T_2:\Gamma_7$ is predominantly non-radiative. Although Altarelli [35] predicted the $\text{Se}^+ 1s:E$ state to lie above $1s:T_2$, the $\text{Se}^+ 1s:E$ state has not yet been experimentally observed. It is conceivable, however highly unusual, that $1s:E$ lies below $1s:T_2$. If $1s:E$ were to lie below $1s:T_2:\Gamma_7$ it could provide a nonradiative decay pathway which could account for the low radiative efficiency of the $1s:T_2:\Gamma_7 \Leftrightarrow 1s:A$ transition.

The $1s:A \Leftrightarrow 1s:E$ transition is both EMT and symmetry-forbidden, in contrast with $1s:A \Leftrightarrow 1s:T_2:\Gamma_7$ which is symmetry-allowed, and so indirect methods are needed to deduce the binding energy of the $1s:E$ state of both Se^0 and Se^+ . In the neutral charge state, Se^0 , the location of the $1s:E$ state has been shown to lie above $1s:T_2$, which for the neutral state Se^0 splits into levels $1s:^1T_2$ and $1s:^3T_2$ (see Ref. [36]). The position of $1s:E$ was extrapolated from strain-induced hybridization of the $1s:E$ and $1s:^1T_2$ levels [36], with a projected unstrained binding energy of 31.4 meV , corresponding to a $1s:A \Leftrightarrow 1s:E$ transition of 2220 cm^{-1} . Here we show the results of Raman spectroscopy in an effort to observe forbidden transitions in both Se^+ and Se^0 , specifically the $1s:A \Leftrightarrow 1s:E$ transition which has been observed for shallow donors [37].

Raman spectra of the $^{28}\text{Si}:^{78}\text{Se}:\text{IB}$ sample [33] were measured using a Bruker IFS 125HR FTIR spectrometer using tunable narrowband 1080 nm ($\sim 9260 \text{ cm}^{-1}$) and 1064 nm ($\sim 9400 \text{ cm}^{-1}$) excitation sources, amplified using an IPG Photonics amplifier (YAR-10K-1064-LP-SF), a CaF_2 beam splitter, and detected using either a liquid nitrogen-cooled Ge diode detector (for Se^0 Raman experiments) or a liquid nitrogen-cooled InSb detector (for Se^+ Raman experiments) with a band-pass filter mounted in the InSb detector's cryogenic assembly to reduce incident room temperature blackbody radiation and increase sensitivity (although the cold-filtered InSb was still much less sensitive than the Ge diode detector). In the detection arm, 1150 and 1200 nm long pass filters were used for laser rejection, with an additional 1100 nm long pass filter used in the Se^0 Raman experiments.

In Fig. 5a we see the results of Raman spectroscopy centred near $(9260 - 2220) \text{ cm}^{-1}$ where we expect to observe Raman features corresponding to the $1s:A \Leftrightarrow 1s:E$ transition of Se^0 when driving with laser light near 1080 nm . We observe a feature which shifts linearly with laser frequency closely matching the projected value for

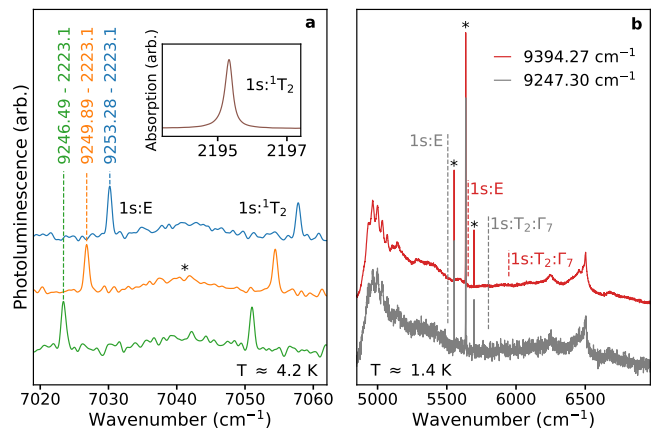


Fig. 5. (a) Raman spectroscopy of the Se^0 region showing features whose shifts in energy match the shifts in tunable laser energy. (Applied laser energy from bottom to top: 9246.49 , 9249.89 , and 9253.28 cm^{-1}). The left (right) peaks correspond to Raman scattering from the $1s:A \Leftrightarrow 1s:E$ ($1s:A \Leftrightarrow 1s:^1T_2$) transition with an average measured offset of 2223.1 cm^{-1} (2195.5 cm^{-1}) from the applied laser energy. A broad photoluminescence feature of unknown origin is labeled by an *. (Inset) The offset due to $1s:A \Leftrightarrow 1s:^1T_2$ matches the observed energy of the $1s:A \Leftrightarrow 1s:^1T_2$ transition seen in absorption. (b) Raman spectroscopy of the Se^+ donor region revealing no signs of $1s:E$ or any other Raman-shifted transitions. Photoluminescence lines corresponding to bound exciton features of unknown origin are marked with an *. Expected Raman feature positions are indicated with dashed lines assuming the theoretically predicted binding energy of $1s:E$ [35] and the known transition energy of $1s:A \Leftrightarrow 1s:T_2:\Gamma_7$. Spectra were collected with a resolution of 1.0 cm^{-1} using a liquid nitrogen-cooled InSb detector with a cryogenically mounted band-pass filter.

the $1s:A \Leftrightarrow 1s:E$ transition. Although unexpected from shallow donor Raman measurements, we also observe a Raman-active feature that matches the measured value of the $1s:A \Leftrightarrow 1s:^1T_2$ transition.

We measure an average shift from the laser position of $2223.1(5) \text{ cm}^{-1}$ corresponding to $1s:A \Leftrightarrow 1s:E$ which agrees with the projected strain-free transition frequency of 2220 cm^{-1} from Ref. [36]. We measure an average shift from the laser position of $2195.5(5) \text{ cm}^{-1}$ which agrees with the $1s:A \Leftrightarrow 1s:^1T_2$ transition energy of $2195.4(5) \text{ cm}^{-1}$ directly observed in absorption (See inset of Fig. 5a).

In Fig. 5b we show the spectral region where one would expect to observe Raman transitions associated with the $1s:A \Leftrightarrow 1s:E$ transitions of Se^+ . Energies labelled $1s:E$, denoted by dashed vertical lines in Fig. 5b, are based on the calculations of Altarelli [35] who predicted the $1s:E$ level of Se^+ to have a binding energy of $\sim 130 \text{ meV}$, corresponding to a $1s:A \Leftrightarrow 1s:E$ transition near 3740 cm^{-1} . We note no observable feature shifts over the broad range we would expect to detect Raman Se^+ transitions. It is possible that $1s:E$ is simply very broad making it ex-

tremely difficult to observe. The $1s:A \Leftrightarrow 1s:T_2:\Gamma_7$ transition was not observed, which agrees with similar shallow donor Raman experiments. The precise binding energy of $1s:E$ level of Se^+ remains the subject of future investigation.

III. CONCLUSION

We have demonstrated that a variety of performance metrics of the $^{77}Se^+$ spin-photon interface, built upon its $1s:A \Leftrightarrow 1s:T_2:\Gamma_7$ transition, are more favourable than previously thought. A number of key properties of this interface were examined and shown to have encouraging features, including long spin T_1 lifetimes exceeding 4.6(1.5) hours at low temperatures and near Earth's magnetic field, a larger transition dipole moment of 1.96(8) Debye, a $1s:T_2:\Gamma_7$ excited state lifetime of 7.7(4) ns, a total radiative efficiency of 0.80(9) %, and a zero phonon line fraction of 16(1) %. These results imply that the spin-dependent cavity cooperativity threshold of 1 may be crossed with routinely achievable photonic cavities having mode volumes of $\sim(\lambda/n)^3$ and Q-factors of 1.5×10^4 . A broad variety of silicon quantum technologies may be built based upon this key and highly

sought-after spin-dependent nonlinearity.

Acknowledgments

The ^{28}Si samples used in this study were prepared from Avo28 crystal produced by the International Avogadro Coordination (IAC) Project (2004-2011) in cooperation among the BIPM, the INRIM (Italy), the IRMM (EU), the NMIA (Australia), the NMIJ (Japan), the NPL (UK), and the PTB (Germany). We thank Eundeok Mun for sealing the quartz ampules used to make the samples. We also thank Dev Sharma for synthesizing the selenium dioxide used to make the samples.

Funding

This work was supported by the Natural Sciences and Engineering Research Council of Canada, the Canada Research Chairs program, the Canada Foundation for Innovation and the British Columbia Knowledge Development Fund.

-
- [1] Zhen-Sheng Yuan, Yu-Ao Chen, Bo Zhao, Shuai Chen, Jörg Schmiedmayer, and Jian-Wei Pan, "Experimental demonstration of a BDCZ quantum repeater node," *Nature* **454**, 98–110 (2008).
- [2] S. T. Yilmaz, P. Fallahi, and A. Imamoglu, "Quantum-dot-spin single-photon interface," *Phys. Rev. Lett.* **105**, 033601 (2010).
- [3] H. Bernien, B. Hensen, W. Pfaff, G. Koolstra, M. S. Blok, L. Robledo, T. H. Taminiau, M. Markham, D. J. Twitchen, L. Childress, and R. Hanson, "Heralded entanglement between solid-state qubits separated by three metres," *Nature* **497**, 86 EP – (2013).
- [4] Kristiaan De Greve, Leo Yu, Peter L. McMahon, Jason S. Pelc, Chandra M. Natarajan, Na Young Kim, Eisuke Abe, Sebastian Maier, Christian Schneider, Martin Kamp, Sven Höfling, Robert H. Hadfield, Alfred Forchel, M. M. Fejer, and Yoshihisa Yamamoto, "Quantum-dot spin-photon entanglement via frequency downconversion to telecom wavelength," *Nature* **491**, 421 EP – (2012).
- [5] Lucio Robledo, Lilian Childress, Hannes Bernien, Bas Hensen, Paul F. A. Alkemade, and Ronald Hanson, "High-fidelity projective read-out of a solid-state spin quantum register," *Nature* **477**, 574 EP – (2011).
- [6] Brendon C. Rose, Ding Huang, Zi-Huai Zhang, Paul Stevenson, Alexei M. Tyryshkin, Sorawis Sangtawesin, Srikanth Srinivasan, Lorne Loudin, Matthew L. Markham, Andrew M. Edmonds, Daniel J. Twitchen, Stephen A. Lyon, and Nathalie P. de Leon, "Observation of an environmentally insensitive solid-state spin defect in diamond," *Science* **361**, 60–63 (2018).
- [7] Tian Zhong, Jonathan M. Kindem, Evan Miyazono, and Andrei Faraon, "Nanophotonic coherent light-matter interfaces based on rare-earth-doped crystals," *Nature Communications* **6**, 8206 EP – (2015), article.
- [8] Manjin Zhong, Morgan P. Hedges, Rose L. Ahlefeldt, John G. Bartholomew, Sarah E. Beavan, Sven M. Wittig, Jevon J. Longdell, and Matthew J. Sellars, "Optically addressable nuclear spins in a solid with a six-hour coherence time," *Nature* **517**, 177 EP – (2015).
- [9] David J. Christle, Paul V. Klimov, Charles F. de las Casas, Krisztián Szász, Viktor Ivády, Valdas Jokubavicius, Jawad Ul Hassan, Mikael Syväjärvi, William F. Koehl, Takeshi Ohshima, Nguyen T. Son, Erik Janzén, Ádám Gali, and David D. Awschalom, "Isolated spin qubits in sic with a high-fidelity infrared spin-to-photon interface," *Phys. Rev. X* **7**, 021046 (2017).
- [10] Matthias Widmann, Sang-Yun Lee, Torsten Rendler, Nguyen Tien Son, Helmut Fedder, Seoyoung Paik, Li-Ping Yang, Nan Zhao, Sen Yang, Ian Booker, Andrej Denisenko, Mohammad Jamali, S. Ali Momenzadeh, Ilja Gerhardt, Takeshi Ohshima, Adam Gali, Erik Janzén, and Jörg Wrachtrup, "Coherent control of single spins in silicon carbide at room temperature," *Nature Materials* **14**, 164 EP – (2014).
- [11] X. Linpeng, M. L. K. Viitaniemi, A. Vishnuradhan, Y. Kozuka, C. Johnson, M. Kawasaki, and K.-M. C. Fu, "Coherence properties of shallow donor qubits in ZnO," *ArXiv e-prints* (2018), arXiv:1802.03483 [quant-ph].
- [12] Kamyar Saeedi, Stephanie Simmons, Jeff Z. Salvail, Phillip Dluhy, Helge Riemann, Nikolai V. Abrosimov, Peter Becker, Hans-Joachim Pohl, John J. L. Morton, and Mike L. W. Thewalt, "Room-temperature quantum bit storage exceeding 39 minutes using ionized donors in silicon-28," *Science* **342**, 830–833 (2013).
- [13] Gary Wolfowicz, Stephanie Simmons, Alexei M. Tyryshkin, Richard E. George, Helge Riemann, Niko-

- lai V. Abrosimov, Peter Becker, Hans-Joachim Pohl, Stephen A. Lyon, Mike L. W. Thewalt, and John J. L. Morton, “Decoherence mechanisms of ^{209}Bi donor electron spins in isotopically pure ^{28}Si ,” *Phys. Rev. B* **86**, 245301 (2012).
- [14] J. T. Muhonen, A. Laucht, S. Simmons, J. P. Dehollain, R. Kalra, F. E. Hudson, S. Freer, K. M. Itoh, D. N. Jamieson, J. C. McCallum, A. S. Dzurak, and A. Morello, “Quantifying the quantum gate fidelity of single-atom spin qubits in silicon by randomized benchmarking,” *Journal of Physics: Condensed Matter* **27**, 154205 (2015).
- [15] Juan P. Dehollain, Stephanie Simmons, Juha T. Muhonen, Rachpon Kalra, Arne Laucht, Fay Hudson, Kohei M. Itoh, David N. Jamieson, Jeffrey C. McCallum, Andrew S. Dzurak, and Andrea Morello, “Bell’s inequality violation with spins in silicon,” *Nature Nanotechnology* **11**, 242 EP – (2015).
- [16] Mohsen K. Akhlaghi, Ellen Schelew, and Jeff F. Young, “Waveguide integrated superconducting single-photon detectors implemented as near-perfect absorbers of coherent radiation,” *Nature Communications* **6**, 8233 EP – (2015), article.
- [17] A. Mekis, S. Gloeckner, G. Masini, A. Narasimha, T. Pinguet, S. Sahni, and P. De Dobbelaere, “A grating-coupler-enabled cmos photonics platform,” *IEEE Journal of Selected Topics in Quantum Electronics* **17**, 597–608 (2011).
- [18] M. Hochberg, N. C. Harris, R. Ding, Y. Zhang, A. Novack, Z. Xuan, and T. Baehr-Jones, “Silicon photonics: The next fabless semiconductor industry,” *IEEE Solid-State Circuits Magazine* **5**, 48–58 (2013).
- [19] M. L. W. Thewalt, A. Yang, M. Steger, D. Karaiskaj, M. Cardona, H. Riemann, N. V. Abrosimov, A. V. Gusev, A. D. Bulanov, I. D. Kovalev, A. K. Kaliteevskii, O. N. Godisov, P. Becker, H. J. Pohl, E. E. Haller, J. W. Ager, and K. M. Itoh, “Direct observation of the donor nuclear spin in a near-gap bound exciton transition: P31 in highly enriched Si^{28} ,” *Journal of Applied Physics* **101**, 081724 (2007).
- [20] Chunming Yin, Milos Rancic, Gabriele G. de Boo, Nikolas Stavrias, Jeffrey C. McCallum, Matthew J. Sellars, and Sven Rogge, “Optical addressing of an individual erbium ion in silicon,” *Nature* **497**, 91 EP – (2013).
- [21] Je-Hyung Kim, Shahriar Aghaeimeibodi, Christopher J. K. Richardson, Richard P. Leavitt, Dirk Englund, and Edo Waks, “Hybrid integration of solid-state quantum emitters on a silicon photonic chip,” *Nano Letters* **17**, 7394–7400 (2017), pMID: 29131963.
- [22] J.C. Swartz, D.H. Lemmon, and R.N. Thomas, “Optical excitation spectra of selenium-doped silicon,” *Solid State Communications* **36**, 331 – 334 (1980).
- [23] H. G. Grimmeiss, E. Janzén, and B. Skarstam, “Electronic properties of selenium-doped silicon,” *Journal of Applied Physics* **51**, 3740–3745 (1980).
- [24] H. G. Grimmeiss, E. Janzén, and K. Larsson, “Multi-valley spin splitting of $1s$ states for sulfur, selenium, and tellurium donors in silicon,” *Phys. Rev. B* **25**, 2627–2632 (1982).
- [25] E. Janzén, R. Stedman, G. Grossmann, and H. G. Grimmeiss, “High-resolution studies of sulfur- and selenium-related donor centers in silicon,” *Phys. Rev. B* **29**, 1907–1918 (1984).
- [26] M. Steger, A. Yang, M. L. W. Thewalt, M. Cardona, H. Riemann, N. V. Abrosimov, M. F. Churbanov, A. V. Gusev, A. D. Bulanov, I. D. Kovalev, A. K. Kaliteevskii, O. N. Godisov, P. Becker, H.-J. Pohl, E. E. Haller, and J. W. Ager, “High-resolution absorption spectroscopy of the deep impurities s and se in ^{28}Si revealing the ^{77}Se hyperfine splitting,” *Phys. Rev. B* **80**, 115204 (2009).
- [27] Roberto Lo Nardo, Gary Wolfowicz, Stephanie Simmons, Alexei M. Tyryshkin, Helge Riemann, Nikolai V. Abrosimov, Peter Becker, Hans-Joachim Pohl, Michael Steger, Stephen A. Lyon, Mike L. W. Thewalt, and John J. L. Morton, “Spin relaxation and donor-acceptor recombination of se^+ in 28-silicon,” *Phys. Rev. B* **92**, 165201 (2015).
- [28] Kevin J. Morse, Rohan J. S. Abraham, Adam DeAbreu, Camille Bowness, Timothy S. Richards, Helge Riemann, Nikolay V. Abrosimov, Peter Becker, Hans-Joachim Pohl, Michael L. W. Thewalt, and Stephanie Simmons, “A photonic platform for donor spin qubits in silicon,” *Science Advances* **3** (2017), 10.1126/sciadv.1700930.
- [29] Gary Wolfowicz, Alexei M. Tyryshkin, Richard E. George, Helge Riemann, Nikolai V. Abrosimov, Peter Becker, Hans-Joachim Pohl, Mike L. W. Thewalt, Stephen A. Lyon, and John J. L. Morton, “Atomic clock transitions in silicon-based spin qubits,” *Nature Nanotechnology* **8**, 881 EP – (2013).
- [30] G. Feher and E. A. Gere, “Electron spin resonance experiments on donors in silicon. ii. electron spin relaxation effects,” *Phys. Rev.* **114**, 1245–1256 (1959).
- [31] Theodore G. Castner, “Raman spin-lattice relaxation of shallow donors in silicon,” *Phys. Rev.* **130**, 58–75 (1963).
- [32] Theodore G. Castner, “Orbach spin-lattice relaxation of shallow donors in silicon,” *Phys. Rev.* **155**, 816–825 (1967).
- [33] See Supplemental Material at [URL will be inserted by publisher] for additional information concerning sample creation, determination of impurity concentration, transition dipole moment and cooperativity calculations, and impurity conversion factors.
- [34] W Mallawaarachchi, A N Davies, R A Beaman, A J Langley, and W Jeremy Jones, “Concentration-modulated Absorption Spectroscopy Part 4.-The Use of Continuous-wave Lasers,” *J. Chem. SOC. Faraday Trans* **2**, 707–722 (1987).
- [35] M. Altarelli, “Excited states of double donors in silicon,” *Physica B+C* **117**, 122–124 (1983).
- [36] G. Grossmann, K. Bergman, and M. Kleverman, “Spectroscopic studies of double donors in silicon,” *Physica B+C* **146**, 30 – 46 (1987).
- [37] G. B. Wright and A. Mooradian, “Raman scattering from donor and acceptor impurities in silicon,” *Phys. Rev. Lett.* **18**, 608–610 (1967).
- [38] G. G. Devyatykh, A. D. Bulanov, A. V. Gusev, I. D. Kovalev, V. A. Krylov, A. M. Potapov, P. G. Sennikov, S. A. Adamchik, V. A. Gavva, A. P. Kotkov, M. F. Churbanov, E. M. Dianov, A. K. Kaliteevskii, O. N. Godisov, H. J. Pohl, P. Becker, H. Riemann, and N. V. Abrosimov, “High-purity single-crystal monoisotopic silicon-28 for precise determination of avogadro’s number,” *Doklady Chemistry* **421**, 157–160 (2008).
- [39] Cheol-Seong Kim, Eiji Ohta, and Makoto Sakata, “Electrical properties of selenium-diffused silicon,” *Japanese Journal of Applied Physics* **18**, 909 (1979).
- [40] E. Schibli and A.G. Milnes, “Deep impurities in silicon,” *Materials Science and Engineering* **2**, 173 – 180 (1967).
- [41] Cheol-Seong Kim and Makoto Sakata, “Diffusion coefficient of selenium in silicon by sheet hall coefficient measurements,” *Japanese Journal of Applied Physics* **18**, 247

- (1979).
- [42] Peter Pichler, *Intrinsic Point Defects, Impurities, and Their Diffusion in Silicon*, 1st ed. (Springer-Verlag Wien, 2004).
- [43] S Zakel, S Wundrack, H Niemann, O Rienitz, and D Schiel, “Infrared spectrometric measurement of impurities in highly enriched ‘si28’,” *Metrologia* **48**, S14 (2011).
- [44] Zhiyi Yu, Y. X. Huang, and S. C. Shen, “Spin-orbit splitting of the valence bands in silicon determined by means of high-resolution photoconductive spectroscopy,” *Phys. Rev. B* **39**, 6287–6289 (1989).
- [45] P. G. Sennikov, T. V. Kotereva, A. G. Kurganov, B. A. Andreev, H. Niemann, D. Schiel, V. V. Emtsev, and H. J. Pohl, “Spectroscopic parameters of the absorption bands related to the local vibrational modes of carbon and oxygen impurities in silicon enriched with 28si, 29si, and 30si isotopes,” *Semiconductors* **39**, 300–307 (2005).
- [46] Robert C. Hilborn, “Einstein coefficients, cross sections, f values, dipole moments, and all that,” *American Journal of Physics* **50**, 982–986 (1982).
- [47] Bradley J Frey, Douglas B Leviton, and Timothy J Madison, “Temperature-dependent refractive index of silicon and germanium,” in *Optomechanical Technologies for Astronomy*, Vol. 6273 (International Society for Optics and Photonics, 2006) p. 62732J.